*Article*

# C$_4$S Nanosheet: A Potential Anode Material for Potassium-Ion Batteries

**Shaohua Lu \*, Enhao Lu, Kai Zhu and Xiaojun Hu \***

College of Materials Science and Engineering, Zhejiang University of Technology, Hangzhou 310014, China
\* Correspondence: lsh@zjut.edu.cn (S.L.); huxj@zjut.edu.cn (X.H.)

**Abstract:** Potassium ion batteries (KIBs) have received increasing popularity owing to their distinct advantages. We discover a hitherto unknown C$_4$S nanosheet, a novel carbon-based material with carbon and sulfur consisting of pentagons and hexagons rings. The proposed C$_4$S nanosheet is highly stable dynamically, thermodynamically, mechanically, and chemically, according to first-principles calculations. Moreover, the graphene-like C$_4$S nanosheet is a prospective KIBs anode material, which has a metallic band structure, a relatively low diffusion barrier (0.07 eV), a large capacity (1340 mA h g$^{-1}$), and an acceptable average voltage (0.44 V). Finally, we demonstrate good cycling stability of the C$_4$S nanosheet. Our findings indicate that the proposed C$_4$S nanosheet is a potentially favorable KIBs anode material.

**Keywords:** potassium ion batteries (KIBs); global structure search; first-principles calculations; two-dimensional (2D) material; the anode material

## 1. Introduction

As portable electronic devices become increasingly ubiquitous and, consequently, the sharp rise of requests for high-performance and cost-effective rechargeable batteries, an enormous amount of effort from the science community is involved in this crucial research [1–3]. Lithium-ion batteries (LIBs) are among the most widely used rechargeable batteries, with applications in portable electronic gadgets, electric automobiles, and grid-scale energy storage systems [4,5]. However, lithium reserves account for only 0.002% of the earth's crust's elemental abundance and are insufficient to meet the continually expanding requirements of future large-scale energy-related applications [6–8]. At the same time, the cost of lithium carbonate, a precursor to LIBs, has been rising due to the widespread use of these batteries [9,10].

To date, potassium-ion batteries (KIBs) have become a more prospective innovative energy storage solution than LIBs for four reasons [4,11,12]. First, the potassium (K) reserves account for more than 1% [13], which enables the comparatively competitive advantages of KIBs in energy storage. Furthermore, potassium carbonate, a predecessor to KIBs, costs only one-sixth as much as LIBs [14,15]. Moreover, KIBs exhibit a low redox potential similar to that of LIBs in non-aqueous solutions [16]. Finally, KIBs have a minor Stokes radius in aqueous or propylene carbonate solutions, allowing them to diffuse rapidly in the electrolyte solution [17–19]. These advantages of KIBs have prompted a growing number of materials to be explored for KIBs applications.

However, the fundamental problem that KIBs face is the big ion radius of K elements, which impedes the access of K ions to the electrodes, leading to poor performance with a slow electron transfer rate, limited capacity, and poor cycle stability throughout the charge and discharge operations [13,20–23]. Moreover, K ions can be de-embedded and inserted into the layered structure of electrodes, causing a limited cycle life due to the volume expansion induced by the increased layer spacing [22–24]. Additionally, the layered skeleton may collapse over certain cycles in the actual ambient environment [25,26]. Therefore, high-performance anode materials are required to overcome these critical challenges.

The advantages of using KIBs anode materials have been demonstrated for two-dimensional (2D) materials [27–29]. Their enormous specific surface area provides plenty of adsorption sites for K ions adsorbed, and the layered structure provides favorable diffusion pathways for the movement of K ions [30]. For example, Sibari et al. demonstrated that potassium has a relatively low diffusion barrier than lithium, as low as 0.02 eV, on the surface of a phosphorene monolayer [31]. Furthermore, 2D materials have superior mechanical properties that ensure the electrode structure remains unchanged during the embedding and peeling of K ions [32]. Graphene is currently one of the most popular 2D materials due to its suitability as an ion storage material. One of the key advantages of graphene is its ability to facilitate fast diffusion of surface ions, making it an excellent choice as an anode material for rechargeable batteries [33–35].

However, graphene has a weak affinity for K ions, making it challenging to apply to KIBs on a large scale [36]. An effective strategy is to search for carbides with a graphene-like structure and simultaneously enhance the affinity for K elements. For example, Mansouri et al. calculated that the theoretical capacity of a graphene/phosphorene hybrid material could reach up to 433 mA h $g^{-1}$ with the presence of phosphorene [37]. Dou et al. demonstrated that the $PC_6$ monolayer enhances the affinity of K ions by the carbon-based material through the addition of P elements and has a low diffusion energy barrier of 0.26 eV for K ions [38]. Bhauriyal et al. explored an experimentally synthesized $C_3N$ structure due to the N element increasing the affinity for K ions with a theoretical capacity of as high as 1072 mA h g $^{-1}$ [39]. However, KIBs' anode materials have not been sufficiently explored to enable their commercialization, and further exploration of anode materials is necessary.

In this work, we discover a dynamically stable monolayered $C_4S$ structure by performing global structure searches. We report that the $C_4S$ nanosheet is a planar structure with a large specific surface area for ion migration on the surface and that there are suitable sites on the surface of the $C_4S$ nanosheet for ion adsorption. Next, we investigate the adsorption of K ions on the $C_4S$ nanosheet using accurate first-principles calculations. Our findings reveal that the $C_4S$ nanosheet has good structural stability, good electrical conductivity, and a high migration rate that has only a 0.07 eV diffusion barrier, which are desirable properties for anode material. Our study demonstrates that the proposed $C_4S$ monolayer exhibits a high theoretical capacity of 1340 mA h $g^{-1}$ and a suitable average open circuit voltage of 0.44 V. As a result, our research indicates that the $C_4S$ nanosheet appears to be a suitable high-performance anode material for KIBs for future practical applications.

## 2. Computational Method

We implemented a 2D global structure search of $C_4S$ with the CALYPSO code, utilizing the particle swarm optimization (PSO) method for global structure optimization [40,41]. To eliminate artifact interactions between adjacent periodic units, a 20 Å vacuum space was inserted in the z-direction for monolayered $C_4S$ structures. The Vienna Ab initio Simulation Package (VASP) was used in our computations, which depend on density functional theory (DFT), and the projector augmented wave (PAW) approach was used as the pseudopotential [42–44]. The generalized gradient approximations (GGA) [45] in the Perdew–Burke–Ernzerhof (PBE) format were used to model the exchange–correlation interactions between valence electrons [46]. The first Brillouin zone was sampled using a $3\times3\times1$ Γ-centered method k-point mesh. The Γ-centered k-point grid frequently saves computing costs and offers useful information about band gaps. The self-consistent electronic computations and the ionic relaxation thresholds were both set to $10^{-7}$ eV and 0.01 eVÅ$^{-1}$, respectively. The band structure of the $C_4S$ monolayer was calculated by Heyd–Scuseria–Ernzerhof functional (HSE06) method with 0.25 exact exchange in a Hartree–Fock-type [47]. We employed the DFT-D2 scheme to examine the vdW interactions between the K ion and $C_4S$ monolayer [48,49]. This interaction is critical, especially when physisorption mechanisms are present. We employed the climbing image nudged elastic band (CI-NEB) approach for calculating the K ion migration pathway and accompanying diffusion energy

barriers on a $2 \times 2$ supercell [50]. To confirm the dynamic stability of selected structures, we performed phonon dispersion calculations by virtue of the phonopy package [51]. Additionally, the thermal stability of predicted materials at elevated temperatures was evaluated using ab initio molecular dynamics (AIMD) simulation in a canonical ensemble thermostated by the Nose–Hoover thermostat [52].

## 3. Results and Discussions

In order to investigate the potential most sTable 2D $C_xS_y$ structure, a comprehensive global structure search was conducted within the $C_xS_y$ system ($x \in [1, 4]$, $y \in [1, 2]$), involving varying cell size and layer thickness. Figure 1a depicts the top and side views of the $C_4S$ nanosheet structure with an optimized lattice constant of 4.42 Å. The $C_4S$ monolayer consists of carbon and sulfur in pentagons and hexagons and is different from graphene, a structure composed solely of carbon hexagonal rings. The C-C bond length was 1.39 Å, comparable to that of graphene, while the C-S bond length was 1.84 Å.
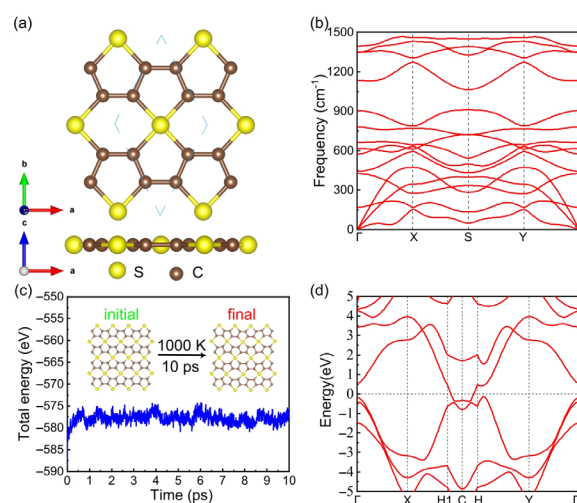


**Figure 1.** (**a**) Top and side views of the optimized configuration of the $C_4S$ monolayer. The blue dashed line shows the original unit cell of $C_4S$. (**b**) Phonon dispersion plot of the $C_4S$ monolayer, showing no imaginary frequencies throughout the Brillouin zone. (**c**) AIMD simulation of the $C_4S$ nanosheet at 1000 K for 10 ps, with before and after top views of the geometric structure. (**d**) Electronic band structure of the $C_4S$ monolayer at the HSE06 levels.

We then explored the stability of the conceived $C_4S$ nanosheet, including dynamical, thermodynamical, mechanical, and chemical stability. The phonon band dispersions of $C_4S$ were first calculated, as illustrated in Figure 1b. Additionally, the phonon band of the $C_4S$ single layer exhibited no imaginary frequency across the whole path of the Brillouin zone, indicating that the $C_4S$ monolayer was dynamical stability. To further assess the thermodynamic stability of the $C_4S$ monolayer, we employed an AIMD simulation with a $4 \times 4$ supercell at a temperature of 1000 K and a simulation time of 10 ps. Figure 1c depicts the initial and final MD images and the total energy variations during the simulation process. The total energy tends to stabilize rapidly, and the final configuration of the $C_4S$ monolayer has no bond breaking or structural rearrangement, which demonstrates that the $C_4S$ monolayer is thermodynamic and stable even under highly elevated temperatures.

In addition, we calculated the stress–strain model to verify the mechanical stability of the structure. The $C_4S$ monolayer exhibits mechanical stability as its elastic constants $C_{11}$, $C_{22}$, $C_{12}$, and $C_{66}$ are 170.14 N m$^{-1}$, 219.23 N m$^{-1}$, 22.02 N m$^{-1}$, and 22.85 N m$^{-1}$, respectively, fulfilling the Born–Huang criteria for 2D nanosheets ($C_{11}C_{22} > C_{12}^2$ and $C_{66} > 0$) [53]. As illustrated in Figure 1d, the HSE06 levels band structure of the $C_4S$ monolayer indicates this structure is metallic in nature.

Chemical stability is another consideration in the practical application of the material in the workplace. For instance, Gao et al. persuasively demonstrated that $MoS_2$ and $WS_2$ monolayers would be eroded to oxidation when exposed to air in the ambient environment [54]. To assess the chemical stability of the $C_4S$ monolayer, we performed AIMD simulations with $O_2$ and a mixture of $O_2$ and $H_2O$ molecules. As shown in Figure 2, the $C_4S$ in the two environments retains its original structure at 300 K during the process of AIMD simulation, and the total energy fluctuation is insubstantial. Our AIMD simulations demonstrate that no chemical reactions occur during the exposure of the $C_4S$ monolayer to oxygen, suggesting that the material is stable in the air.
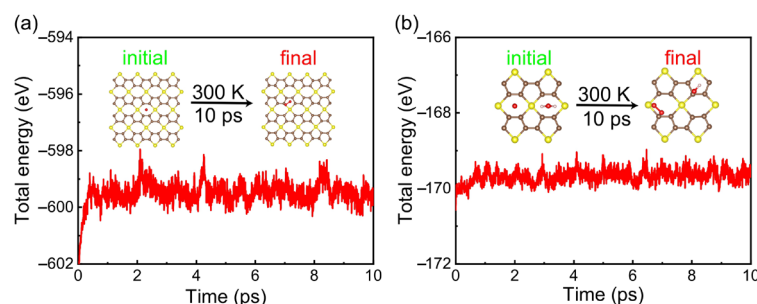


**Figure 2.** Energy fluctuation of the $C_4S$ monolayer upon exposure to (**a**) an $O_2$ molecule and (**b**) a mixture of $O_2$ and $H_2O$ molecules, as determined by AIMD simulations.

For KIBs, the effective rate of the charge–discharge process is determined by the diffusion rate of K ions on the anode material surface. Therefore, we investigate the adsorption and diffusion properties of isolated K ions on the surface of the $C_4S$ monolayer. We exhaustively consider seven possible adsorption sites, as shown in Figure S1. They are named $P_n$ (n = 1, 2, 3, 4, 5, 6, and 7). $P_1$ is located on the top of the S atom, $P_2$ is located on the top of the C atom, $P_3$ and $P_4$ are located on the hollow positions of the pentagon and hexagon composed of S and C atoms, $P_5$ and $P_6$ are the bridge positions of the two difference C-C bonds, $P_7$ is the bridge position of the C-S bond. The following reaction could be utilized to demonstrate the process of ionic adsorption:

$$C_4S + xK^+ + xe^- \leftrightarrow C_4SK_x \tag{1}$$
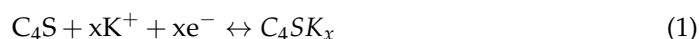
During the charging process, K ions and electrons are transferred from the cathode material to the anode material, resulting in a K-loaded $C_4S$ anode. It is noteworthy that the contribution of volume and entropy to the average adsorption energy can be deemed insignificant. To discern the optimal configuration of the K atom on the monolayer, we employ the adsorption energy ($E_{ad}$) equation for evaluation:

$$E_{ad} = \frac{E_{total} - n_K\mu_K - E_{C_4S}}{n_K} \tag{2}$$

where $E_{total}$, $\mu_K$, and $E_{C_4S}$ are the total energy of K absorbed $C_4S$ monolayer, a K atom in bulk with bcc lattice, and $C_4S$ monolayer, respectively. Furthermore, the number of adsorbed K ions is denoted as $n_K$.

More negative adsorption energy is advantageous, indicating that the isolated K atom has a preference for adsorption on the $C_4S$ monolayer rather than clustering with other metal atoms. This behavior is advantageous for achieving a higher battery capacity [55]. Two more stable adsorption sites were discovered after structural relaxation: $P_3$ (pentagonal center) and $P_4$ (hexagonal center). To prevent the formation of metal clusters and achieve a desirable working voltage, we calculated the adsorption energies to be −0.85 and −0.93 eV, respectively. These negative adsorption energies indicate that the isolated K atom exhibits a strong preference for adsorption on the $C_4S$ monolayer rather than clustering with other metal atoms. Khan et al. showed that the binding energy of calcium lower than cohesive

energy in $C_2N$ could also prevent metal clusters from forming. The calculated binding energies of these two adsorption sites are −1.86 and −1.77 eV, respectively, which are much higher than the cohesive energies of potassium (−0.93 eV) [37,56,57]. Therefore, it can be proved that the surface of $C_4S$ can prevent potassium clusters from each other when used as anode materials for potassium ion batteries.

To better understand the adsorption behaviors of K ions, we calculated the differential charge density between the K ions and the $C_4S$ nanosheet, as illustrated in Figure 3a,b. Electrons are transferred from the K ions to the $C_4S$ nanosheet, leading to a local electron accumulation in the six-membered ring beneath the K atom. The electrostatic repulsion between the C-C and the C-S bonds results in an increase in the bond length, the C-S bond length increases from 1.84 to 1.89 Å, and the C-C bond length increases from 1.39 to 1.41 Å.
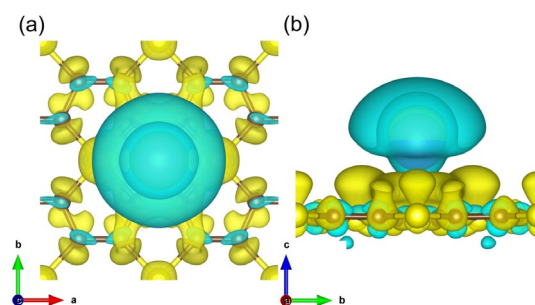


**Figure 3.** Plots of the charge density difference for the K atom on the $C_4S$ surface from (**a**) top views and (**b**) side views. The blue areas are electrons consumed, and the yellow areas represent electrons accumulate.

Then, we evaluated the diffusion energy barrier of K ions on the $C_4S$ monolayer by the CI-NEB method. We examined multiple migration pathways to determine the diffusion mechanism of K ions, taking into account the structural symmetry and preferred adsorption sites of the material. Two highly possible migration paths are shown in Figure 4a. Path I involves the direct movement of the K ion from the hexagonal center site to the adjacent hexagonal center, which represents the shortest migration path between the two hexagonal center sites ($P_4$). While on path II involves the K ion moving from the pentagonal center site ($P_3$) to the nearest neighboring pentagonal center site. The diffusion energy barriers for K ion diffusion along path I and path II were found to be 0.19 and 0.07 eV, respectively. These results suggest that K ions tend to diffuse along path II, which is more favorable due to the lower diffusion energy barrier. Additionally, the diffusion barrier of 0.07 eV is considerably lower than that of other 2D KIBs anode materials, such as graphene (0.12 eV) [58], SiGe (0.14 eV) [59], $PC_6$ (0.26 eV) [38], $Ti_2BN_2$ (0.37 eV) [60], and $Si_2Se_2$ (0.17 eV) [61]. Therefore, the proposed $C_4S$ monolayer should have a satisfactory conductivity that ensures fast K ion transportation.
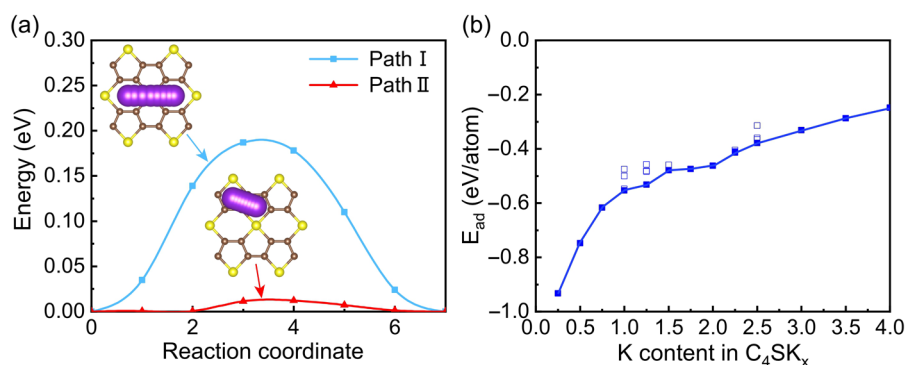


**Figure 4.** (**a**) The energy landscape depicting the relative energy profile of K diffusion along path I and path II on the $C_4S$ monolayer. (**b**) Adsorption energies as the function of K content in $C_4SK_x$.

The amount of K ions adsorbed on the monolayer immediately correlates with the storage capacity, which is also closely related to the performance of KIBs anode materials. To investigate the maximum theoretical capacity and simulate the charging process, we sequentially loaded K ions onto both sides of the $C_4S$ nanosheet. Additionally, we calculated the average adsorption energy of different K ions concentrations to evaluate their structural stability after adsorption. The K ions can be adsorbed stably with negative energy. The adsorption energy of each intermediate configuration was calculated, and the optimal configuration was identified based on the one with the lowest energy at the given concentration, and the results are shown in Figure 4b and Figure S2. We can observe that when the concentration of K ions rises, the repulsion between ions increases, and the value of adsorption energy rises step by step. Finally, we found that the $C_4S$ monolayer of $2 \times 2$ supercell can adsorb up to 16 K ions, and the adsorption energy at the highest concentration of the $C_4SK_4$ is $-0.25$ eV.

The formation energy of the $C_4SK_x$ system was then determined using the following formula to assess the voltage distribution of the $C_4S$ monolayer [62]:

$$E_f = E_{C_4SK_x} - \left[ \frac{XE_{C_4SK_4} + (4-X)E_{C_4S}}{4} \right] \tag{3}$$

where $E_{C_4SK_x}$ is the total energy after $x$ K ions are adsorbed, the value of $x$ is chosen from 0 to 4, and the intermediate increment is 0.25. According to the calculation results, we identified the most energetically advantageous configuration for each concentration condition, and the convex hull for the relative stability of $C_4SK_x$ configurations is shown in Figure 5a. There are six spots on the convex hull, and the values of $K_x$ are 0.25, 0.5, 1.25, 2, 3, 3.5, and 4. These configurations can be considered thermodynamically stable. It is possible to determine the voltage profile between neighboring K concentrations along the structure by investigating the slopes of the convex hull.
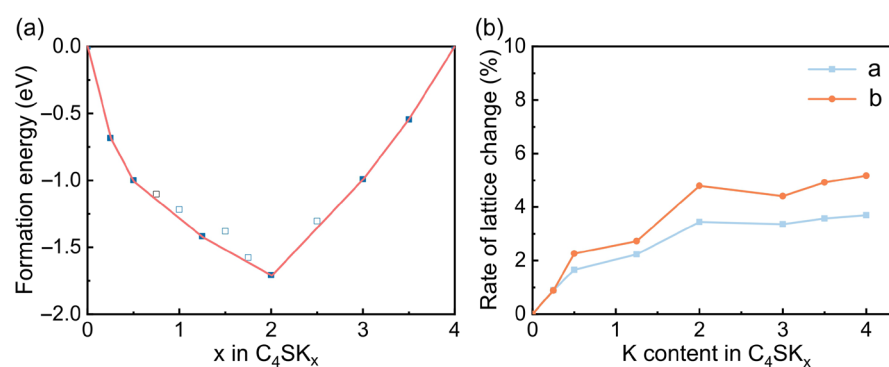


**Figure 5.** (**a**) The fluctuations of formation energy as a function of $x$ in $C_4SK_x$. The red line represents the convex hull for stable phases of $C_4SK_x$. Solid and hollow squares represent thermodynamically stable and unstable structures, respectively. (**b**) Rate of lattice change in a and b direction as the function of K content in $C_4SK_x$.

After investigating the adsorption behavior of K ions, we explored the structural integration of the charge–discharge mechanism. Considering that the charge and discharge processes may cause lattice expansion of the $C_4S$ nanosheet, we calculated the lattice expansion rate in the directions of a and b, as shown in Figure 5b. The figure proves that the b-direction lattice expansion rate is slightly higher than the a-direction lattice expansion rate, which is determined by the increase in the C-S bond length. The lattice constant of the $C_4SK_4$ is 8.13 Å for a and 8.35 Å for b. To simulate the lattice changes after the discharge process, we optimized the monolayer structure after the removal of K ions. The results show that a = 7.83 Å and b = 7.93 Å, which are quite close to the values of the initial $C_4S$ monolayer (7.83 and 7.92 Å, respectively). Therefore, the lattice automatically shrinks after discharge, nearly returning to the original lattice structure, proving that the $C_4S$ lattice

does not distort after absorbing a large number of K ions. This indicates a long charge and discharge cycle life, demonstrating the practicality of the $C_4S$ nanosheet as a KIBs anode material.

The energy storage capacity of rechargeable batteries has received much attention in practical applications. To obtain the theoretical specific capacity, we utilized the following equation:

$$C = \frac{Z_x F}{M_{C_4 S}} \tag{4}$$

where $Z$ represents the positive valence of K ions, $x$ represents the stoichiometric number of adsorbed K, $F$ represents the Faraday constant (26.801 A h mol$^{-1}$), and $M$ represents the molar weight of the $C_4S$ nanosheet of $2 \times 2$ supercell. As depicted in Figure 6a, the theoretical capacity of the $C_4S$ nanosheet is remarkable, reaching up to 1340 mA h g$^{-1}$. The lightweight S and C atoms are responsible for the theoretical storage capacity, and polyatomic adsorption increases the total valence state inside the system. Notably, the theoretical capacity of the $C_4S$ nanosheet expressively surpasses that of other KIBs anode materials, such as the graphene of KIBs (350 mA h g$^{-1}$) [63], the $P_2C_3$ monolayer (729.28 mA h g$^{-1}$) [64], and the $Si_3C$ monolayer (836 mA h g$^{-1}$) [65]. The remarkable theoretical capacity of the $C_4S$ nanosheet underscores its outstanding potential as a promising anode material for KIBs.
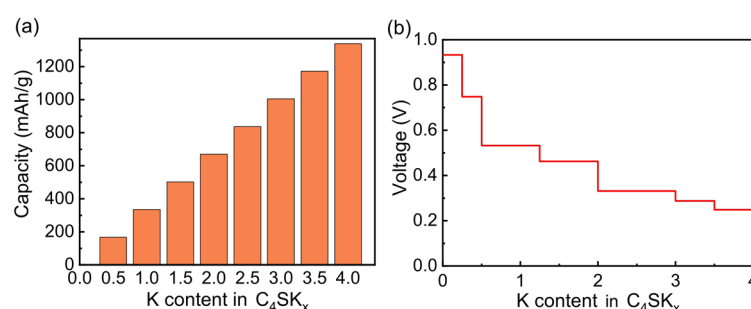


**Figure 6.** (**a**) The relationship between theoretical capacities and K content in $C_4SK_x$. (**b**) The relationship between open circulates voltage and K content in $C_4SK_x$.

To enhance the capability of KIBs' anode materials, the open circuit voltage (*OCV*) is a significant indicator to consider. The average *OCV* can be obtained by:

$$OCV \approx \frac{n_K \mu_K + E_{C_{16}S_4} - E_{total}}{n_K e} \tag{5}$$

Figure 6b displays the *OCV* calculation results for the $C_4S$ nanosheet with varying K adsorption concentrations. The adsorption process shows three distinct voltage plateaus at concentrations of 0.25, 0.50, and 2.00. At 0.25 concentration, the voltage drops from 0.93 to 0.74 V. At 0.50 and 2.00 concentrations, the voltage drops to 0.53 and 0.46 V, respectively, before finally dropping to 0.24 V. Additionally, the voltage is always positive throughout the reaction process, indicating that the reaction can proceed spontaneously to a concentration of 4. The average voltage value calculated through the entire area is 0.44 V, and the ideal range of KIBs is between 0.1 and 1 V, which can provide satisfactory working voltage and higher energy density in KIBs.

To further explore the cycle stability of the $C_4S$ monolayer, we calculated the change in bond length after the fulfilled adsorption of K ions to discover the stability of the charge/discharge process on the structure and perform AIMD simulations at 300 K to determine the thermodynamic stability of the saturated ($C_4SK_4$) concentrations [66,67]. The most critical factor for cyclic stability is the extension of bond length deformation, in which much deformation may cause structural damage after increased charge and discharge cycles, reducing its service life [68]. The optimized geometric configuration remains nearly unchanged at diluted ($C_4SK_{0.25}$) and saturated concentrations, the C-S bond lengths around

K ions are 1.89 (increased by 2.7%) and 1.98 Å (increased by 7.6%), and the lengths of C-C bond are 1.41 (increased by 1.4%) and 1.38 Å (decreased by 0.7%), indicating outstanding cycling stability of the $C_4S$ monolayer. Throughout the AIMD simulation, the total energy of $C_4SK_4$ keeps equilibrium quickly over a period of 10 ps and varies about −164 eV (see Figure 7). The substrate of the $C_4SK_4$ configuration has only minor changes with no significant bond breaking and no release of K ions. Therefore, it can be demonstrated that $C_4SK_4$ should have a prolonged service life.
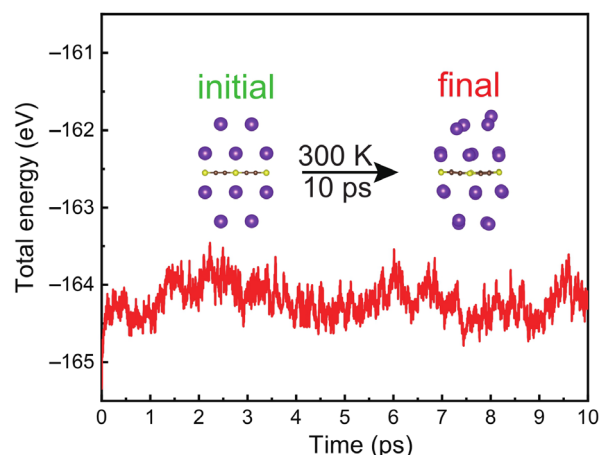


**Figure 7.** The total energy of the saturated concentrations of $C_4SK_4$ fluctuates during the AIMD simulation at 300 K. The side view of the $C_4SK_4$ configuration at the initial and final AIMD simulation is also presented.

## 4. Conclusions

In conclusion, we discovered that the potential of the $C_4S$ nanosheet is a novel and prospective KIBs anode material by utilizing global structure and first-principles calculations. Our study demonstrates the following key findings: (1) the $C_4S$ nanosheet has a metallic band structure with good electrical conductivity; (2) the diffusion barrier for K atoms in the $C_4S$ monolayer is 0.07 eV; (3) the specific capacity (1340 mA h $g^{-1}$) of KIBs, surpassing many others 2D anode material, and can be restored to the original crystal lattice during the discharge process; and (4) the average OCV is 0.44 V within the ideal voltage interval. The advantages of the proposed $C_4S$ monolayer include high specific capacity, high migration rate, and long charge and discharge cycle life, which is a potentially appealing anode material for KIBs.

## References

1. Shi, T.; Li, G.; Han, Y.; Gao, Y.; Wang, F.; Hu, Z.; Cai, T.; Chu, J.; Song, Z. Oxidized indanthrone as a cost-effective and high-performance organic cathode material for rechargeable lithium batteries. *Energy Storage Mater.* **2022**, *50*, 265–273. [CrossRef]
2. Wu, X.; Markir, A.; Xu, Y.; Zhang, C.; Leonard, D.P.; Shin, W.; Ji, X. A rechargeable battery with an iron metal anode. *Adv. Funct. Mater.* **2019**, *29*, 1900911. [CrossRef]
3. Wang, S.B.; Ran, Q.; Yao, R.Q.; Shi, H.; Wen, Z.; Zhao, M.; Lang, X.Y.; Jiang, Q. Lamella-nanostructured eutectic zinc–aluminum alloys as reversible and dendrite-free anodes for aqueous rechargeable batteries. *Nat. Commun.* **2020**, *11*, 1634. [CrossRef]
4. Kim, H.; Kim, J.C.; Bianchini, M.; Seo, D.H.; Rodriguez-Garcia, J.; Ceder, G. Recent progress and perspective in electrode materials for K-ion batteries. *Adv. Energy Mater.* **2018**, *8*, 1702384. [CrossRef]
5. Lee, W.; Muhammad, S.; Sergey, C.; Lee, H.; Yoon, J.; Kang, Y.M.; Yoon, W.S. Advances in the cathode materials for lithium rechargeable batteries. *Angew. Chem. Int. Ed.* **2020**, *59*, 2578–2605. [CrossRef]
6. Borah, R.; Hughson, F.; Johnston, J.; Nann, T. On battery materials and methods. *Mater. Today Adv.* **2020**, *6*, 100046. [CrossRef]
7. Jie, Y.; Tan, Y.; Li, L.; Han, Y.; Xu, S.; Zhao, Z.; Cao, R.; Ren, X.; Huang, F.; Lei, Z.; et al. Electrolyte solvation manipulation enables unprecedented room-temperature calcium-metal batteries. *Angew. Chem. Int. Ed.* **2020**, *59*, 12689–12693. [CrossRef]
8. Li, Y.; Gao, X.; Feng, X.; Ren, D.; Li, Y.; Hou, J.; Wu, Y.; Du, J.; Lu, L.; Ouyang, M. Battery eruption triggered by plated lithium on an anode during thermal runaway after fast charging. *Energy* **2022**, *239*, 122097. [CrossRef]
9. Vaalma, C.; Giffin, G.A.; Buchholz, D.; Passerini, S. Non-aqueous K-ion battery based on layered $K_{0.3}MnO_2$ and hard carbon/carbon black. *J. Electrochem. Soc.* **2016**, *163*, A1295. [CrossRef]
10. Hounjet, L.J. Comparing lithium- and sodium-ion batteries for their applicability within energy storage systems. *Energy Storage* **2022**, *4*, e309. [CrossRef]
11. Dong, Y.; Yan, C.; Zhao, H.; Lei, Y. Recent Advances in 2D Heterostructures as Advanced Electrode Materials for Potassium-Ion Batteries. *Small Struct.* **2022**, *3*, 2100221. [CrossRef]
12. Rajagopalan, R.; Tang, Y.; Ji, X.; Jia, C.; Wang, H. Advancements and challenges in potassium ion batteries: A comprehensive review. *Adv. Funct. Mater.* **2020**, *30*, 1909486. [CrossRef]
13. Zhang, W.; Liu, Y.; Guo, Z. Approaching high-performance potassium-ion batteries via advanced design strategies and engineering. *Sci. Adv.* **2019**, *5*, eaav7412. [CrossRef] [PubMed]
14. Wang, X.; Wang, H. Designing carbon anodes for advanced potassium-ion batteries: Materials, modifications, and mechanisms. *Adv. Powder Mater.* **2022**, *1*, 100057. [CrossRef]
15. Zhang, Y.; Liu, C.; Wu, Z.; Manaig, D.; Freschi, D.J.; Wang, Z.; Liu, J. Enhanced potassium storage performance for K-Te batteries via electrode design and electrolyte salt chemistry. *ACS Appl. Mater. Interfaces* **2021**, *13*, 16345–16354. [CrossRef]
16. Komaba, S.; Hasegawa, T.; Dahbi, M.; Kubota, K. Potassium intercalation into graphite to realize high-voltage/high-power potassium-ion batteries and potassium-ion capacitors. *Electrochem. Commun.* **2015**, *60*, 172–175. [CrossRef]
17. Yin, H.; Han, C.; Liu, Q.; Wu, F.; Zhang, F.; Tang, Y. Recent advances and perspectives on the polymer electrolytes for sodium/potassium-ion batteries. *Small* **2021**, *17*, 2006627. [CrossRef]
18. Xu, Y.; Dong, H.; Zhou, M.; Zhang, C.; Wu, Y.; Li, W.; Dong, Y.; Lei, Y. Ammonium vanadium bronze as a potassium-ion battery cathode with high rate capability and cyclability. *Small Methods* **2019**, *3*, 1800349. [CrossRef]
19. Zhang, X.; Wei, Z.; Dinh, K.N.; Chen, N.; Chen, G.; Du, F.; Yan, Q. Layered oxide cathode for potassium-ion battery: Recent progress and prospective. *Small* **2020**, *16*, 2002700. [CrossRef]
20. Dhir, S.; Wheeler, S.; Capone, I.; Pasta, M. Outlook on K-ion batteries. *Chem* **2020**, *6*, 2442–2460. [CrossRef]
21. Liang, Y.; Luo, C.; Wang, F.; Hou, S.; Liou, S.C.; Qing, T.; Li, Q.; Zheng, J.; Cui, C.; Wang, C. An organic anode for high temperature 303 potassium-ion batteries. *Adv. Energy Mater.* **2019**, *9*, 1802986. [CrossRef]
22. Xu, J.; Dou, S.; Cui, X.; Liu, W.; Zhang, Z.; Deng, Y.; Hu, W.; Chen, Y. Potassium-based electrochemical energy storage devices: Development status and future prospect. *Energy Storage Mater.* **2021**, *34*, 85–106. [CrossRef]
23. Fan, S.S.; Liu, H.P.; Liu, Q.; Ma, C.S.; Yi, T.F. Comprehensive insights and perspectives into the recent progress of electrode materials for non-aqueous K-ion battery. *J. Mater.* **2020**, *6*, 431–454. [CrossRef]
24. Zhang, L.; Wang, W.; Lu, S.; Xiang, Y. Carbon anode materials: A detailed comparison between Na-ion and K-ion batteries. *Adv. Energy Mater.* **2021**, *11*, 2003640. [CrossRef]
25. Liu, G.; Cao, Z.; Zhou, L.; Zhang, J.; Sun, Q.; Hwang, J.Y.; Cavallo, L.; Wang, L.; Sun, Y.K.; Ming, J. Additives Engineered Nonflammable Electrolyte for Safer Potassium Ion Batteries. *Adv. Funct. Mater.* **2020**, *30*, 2001934. [CrossRef]
26. Naylor, A.J.; Carboni, M.; Valvo, M.; Younesi, R. Interfacial reaction mechanisms on graphite anodes for K-ion batteries. *ACS Appl. Mater. Interfaces* **2019**, *11*, 45636–45645. [CrossRef]
27. Zhao, S.; Guo, Z.; Yan, K.; Guo, X.; Wan, S.; He, F.; Sun, B.; Wang, G. The rise of prussian blue analogs: Challenges and opportunities for high-performance cathode materials in potassium-ion batteries. *Small Struct.* **2021**, *2*, 2000054. [CrossRef]
28. He, X.; Wang, R.; Yin, H.; Zhang, Y.; Chen, W.; Huang, S. 1T-$MoS_2$ monolayer as a promising anode material for (Li/Na/Mg)-ion batteries. *Appl. Surf. Sci.* **2022**, *584*, 152537. [CrossRef]
29. Dong, Y.; Xu, Y.; Li, W.; Fu, Q.; Wu, M.; Manske, E.; Kröger, J.; Lei, Y. Insights into the crystallinity of layer-structured transition metal dichalcogenides on potassium ion battery performance: A case study of molybdenum disulfide. *Small* **2019**, *15*, 1900497. [CrossRef] [PubMed]

30. Zhang, C.; Pan, H.; Sun, L.; Xu, F.; Ouyang, Y.; Rosei, F. Progress and perspectives of 2D materials as anodes for potassium-ion batteries. *Energy Storage Mater.* **2021**, *38*, 354–378. [CrossRef]

31. Sibari, A.; Kerrami, Z.; Kara, A.; Hamedoun, M.; Benyoussef, A.; Mounkachi, O.; Benaissa, M. Adsorption and diffusion on a phosphorene monolayer: A DFT study. *J. Solid State Electrochem.* **2018**, *22*, 11–16. [CrossRef]

32. Xu, Y.; Bahmani, F.; Zhou, M.; Li, Y.; Zhang, C.; Liang, F.; Kazemi, S.H.; Kaiser, U.; Meng, G.; Lei, Y. Enhancing potassium-ion battery performance by defect and interlayer engineering. *Nanoscale Horiz.* **2019**, *4*, 202–207. [CrossRef]

33. Huang, H.; Shi, H.; Das, P.; Qin, J.; Li, Y.; Wang, X.; Su, F.; Wen, P.; Li, S.; Lu, P.; et al. The chemistry and promising applications of graphene and porous graphene materials. *Adv. Funct. Mater.* **2020**, *30*, 1909035. [CrossRef]

34. Wang, B.; Ruan, T.; Chen, Y.; Jin, F.; Peng, L.; Zhou, Y.; Wang, D.; Dou, S. Graphene-based composites for electrochemical energy storage. *Energy Storage Mater.* **2020**, *24*, 22–51. [CrossRef]

35. Chen, K.T.; Chong, S.; Yuan, L.; Yang, Y.C.; Tuan, H.Y. Conversion-alloying dual mechanism anode: Nitrogen-doped carbon-coated $Bi_2Se_3$ wrapped with graphene for superior potassium-ion storage. *Energy Storage Mater.* **2021**, *39*, 239–249. [CrossRef]

36. Musielak, M.; Gagor, A.; Zawisza, B.; Talik, E.; Sitko, R. Graphene oxide/carbon nanotube membranes for highly efficient removal of metal ions from water. *ACS Appl. Mater. Interfaces* **2019**, *11*, 28582–28590. [CrossRef]

37. Mansouri, Z.; Sibari, A.; Al-Shami, A.; Lahbabi, S.; El Kenz, A.; Benyoussef, A.; El Fatimy, A.; Mounkachi, O. Graphene/ Phosphorene nano-heterostructure as a potential anode material for (K/Na)-ion batteries: Insights from DFT and AIMD. *Comput. Mater. Sci.* **2022**, *202*, 110936. [CrossRef]

38. Dou, K.; Ma, Y.; Zhang, T.; Huang, B.; Dai, Y. Prediction of two-dimensional PC6 as a promising anode material for potassium-ion batteries. *Phys. Chem. Chem. Phys.* **2019**, *21*, 26212–26218. [CrossRef] [PubMed]

39. Bhauriyal, P.; Mahata, A.; Pathak, B. Graphene-like carbon–nitride monolayer: A potential anode material for Na- and K-ion batteries. *J. Phys. Chem. C* **2018**, *122*, 2481–2489. [CrossRef]

40. Wang, Y.; Lv, J.; Zhu, L.; Lu, S.; Yin, K.; Li, Q.; Wang, H.; Zhang, L.; Ma, Y. Materials discovery via CALYPSO methodology. *J. Phys. Condens. Mater.* **2015**, *27*, 203203. [CrossRef]

41. Lu, S.; Wang, Y.; Liu, H.; Miao, M.S.; Ma, Y. Self-assembled ultrathin nanotubes on diamond (100) surface. *Nat. Commun.* **2014**, *5*, 3666. [CrossRef] [PubMed]

42. Hafner, J. Ab-initio simulations of materials using VASP: Density-functional theory and beyond. *J. Comput. Chem.* **2008**, *29*, 2044–2078. [CrossRef]

43. Parr, R.G. Density functional theory of atoms and molecules. In Proceedings of the Horizons of Quantum Chemistry: Proceedings of the Third International Congress of Quantum Chemistry, Kyoto, Japan, 29 October–3 November 1979; Springer: Berlin/Heidelberg, Germany, 1980; pp. 5–15.

44. Blöchl, P.E. Projector augmented-wave method. *Phys. Rev. B* **1994**, *50*, 17953. [CrossRef] [PubMed]

45. Perdew, J.P.; Burke, K.; Ernzerhof, M. Generalized gradient approximation made simple. *Phys. Rev. Lett.* **1996**, *77*, 3865. [CrossRef]

46. Hammer, B.; Hansen, L.B.; Nørskov, J.K. Improved adsorption energetics within density-functional theory using revised Perdew-Burke-Ernzerhof functionals. *Phys. Rev. B* **1999**, *59*, 7413. [CrossRef]

47. Heyd, J.; Scuseria, G.E.; Ernzerhof, M. Hybrid functionals based on a screened Coulomb potential. *J. Chem. Phys.* **2003**, *118*, 8207–8215. [CrossRef]

48. Grimme, S. Semiempirical GGA-type density functional constructed with a long-range dispersion correction. *J. Comput. Chem.* **2006**, *27*, 1787–1799. [CrossRef]

49. Bucko, T.; Hafner, J.; Lebegue, S.; Angyan, J.G. Improved description of the structure of molecular and layered crystals: Ab initio DFT calculations with van der Waals corrections. *J. Phys. Chem. A* **2010**, *114*, 11814–11824. [CrossRef]

50. Henkelman, G.; Uberuaga, B.P.; Jónsson, H. A climbing image nudged elastic band method for finding saddle points and minimum energy paths. *J. Chem. Phys.* **2000**, *113*, 9901–9904. [CrossRef]

51. Togo, A.; Oba, F.; Tanaka, I. First-principles calculations of the ferroelastic transition between rutile-type and $CaCl_2$-type $SiO_2$ at high pressures. *Phys. Rev. B* **2008**, *78*, 134106. [CrossRef]

52. Martyna, G.J.; Klein, M.L.; Tuckerman, M. Nosé–Hoover chains: The canonical ensemble via continuous dynamics. *J. Chem. Phys.* **1992**, *97*, 2635–2643. [CrossRef]

53. Born, M.; Huang, K.; Lax, M. Dynamical theory of crystal lattices. *Am. J. Phys.* **1955**, *23*, 474. [CrossRef]

54. Gao, J.; Li, B.; Tan, J.; Chow, P.; Lu, T.M.; Koratkar, N. Aging of transition metal dichalcogenide monolayers. *ACS Nano* **2016**, *10*, 2628–2635. [CrossRef]

55. Lei, S.; Chen, X.; Xiao, B.; Zhang, W.; Liu, J. Excellent electrolyte wettability and high energy density of $B_2S$ as a two-dimensional Dirac anode for non-lithium-ion batteries. *ACS Appl. Mater. Interfaces* **2019**, *11*, 28830–28840. [CrossRef]

56. Poole, R. Cohesive energy of the alkali metals. *Am. J. Phys.* **1980**, *48*, 536–538. [CrossRef]

57. Khan, S.; Mushtaq, M.; Berdiyorov, G.R.; Tit, N. Relevance of metal (Ca versus Mn) embedded C2N for energy-storage applications: Atomic-scale study. *Int. J. Hydrogen Energy* **2021**, *46*, 2445–2463. [CrossRef]

58. Nakada, K.; Ishii, A. Migration of adatom adsorption on graphene using DFT calculation. *Solid State Commun.* **2011**, *151*, 13–16. [CrossRef]

59. Sannyal, A.; Ahn, Y.; Jang, J. First-principles study on the two-dimensional siligene (2D SiGe) as an anode material of an alkali metal ion battery. *Comput. Mater. Sci.* **2019**, *165*, 121–128. [CrossRef]

60. Liang, B.; Ma, N.; Wang, Y.; Wang, T.; Fan, J. N-functionalized Ti$_2$B MBene as high-performance anode materials for sodium-ion batteries: A DFT study. *Appl. Surf. Sci.* **2022**, *599*, 153927. [CrossRef]

61. Wang, J.; Wu, H.; Liu, Z.; Pan, M.; Huang, Z.; Pan, L.; Han, L.; Zhang, K.; Zhao, Y.; Deng, H. Theoretically evaluating two-dimensional tetragonal Si$_2$Se$_2$ and SiSe$_2$ nanosheets as anode materials for alkali metal-ion batteries. *Phys. Chem. Chem. Phys.* **2022**, *24*, 26241–26253. [CrossRef]

62. Shukla, V.; Araujo, R.B.; Jena, N.K.; Ahuja, R. The curious case of two dimensional Si$_2$BN: A high-capacity battery anode material. *Nano Energy* **2017**, *41*, 251–260. [CrossRef]

63. Share, K.; Cohn, A.P.; Carter, R.; Rogers, B.; Pint, C.L. Role of nitrogen-doped graphene for improved high-capacity potassium ion battery anodes. *ACS Nano* **2016**, *10*, 9738–9744. [CrossRef] [PubMed]

64. Hu, Y.; Wang, J.; Lin, H. Metallic two-dimensional P$_2$C$_3$: A promising flexible anode for high-performance potassium-ion batteries. *Colloids Surf. A Physicochem. Eng. Asp.* **2021**, *619*, 126536. [CrossRef]

65. Wang, Y.; Li, Y. Ab initio prediction of two-dimensional Si$_3$C enabling high specific capacity as an anode material for Li/Na/K-ion batteries. *J. Mater. Chem. A* **2020**, *8*, 4274–4282. [CrossRef]

66. Sun, Q.; Dai, Y.; Ma, Y.; Jing, T.; Wei, W.; Huang, B. Ab initio prediction and characterization of Mo$_2$C monolayer as anodes for lithium-ion and sodium-ion batteries. *J. Phys. Chem. Lett.* **2016**, *7*, 937–943. [CrossRef] [PubMed]

67. Ling, C.; Mizuno, F. Boron-doped graphene as a promising anode for Na-ion batteries. *Phys. Chem. Chem. Phys.* **2014**, *16*, 10419–10424. [CrossRef] [PubMed]

68. Arico, A.S.; Bruce, P.; Scrosati, B.; Tarascon, J.M.; Van Schalkwijk, W. Nanostructured materials for advanced energy conversion and storage devices. *Nat. Mater.* **2005**, *4*, 366–377. [CrossRef]